Materials Horizons

Accepted Manuscript

This article can be cited before page numbers have been issued, to do this please use: A. Ghosh, I. Dahan, B. Santra, G. Vijayan, M. Uzhansky and E. Koren*, Mater. Horiz.*, 2026, DOI: 10.1039/D5MH02349A.

ROYAL SOCIETY OF CHEMISTRY

rsc.li/materials-horizons

View Article Online
DOI: 10.1039/D5MH02349A

Visual synaptic devices hold great promise for advanced neuromorphic hardware, offering a viable solution to the von Neumann bottleneck. Yet, most of the reported visual synaptic devices involve hybrid manipulation approaches, which require both optical and electrical stimuli, introducing similar challenges such as complex device architecture, computational latency and high-power consumption. In this work, we demonstrate fully optical controlled operation using a 2D heterostructure neuromorphic device consisting of few-layer $PdSe_2$ and α-In_2Se_3. In particular, the device emulates multiple forms of spike-dependent plasticity, with excitatory and inhibitory synaptic responses in 642–980 nm and 406–520 nm spectral range, respectively. In addition, by leveraging the coupled ferroelectric and optical properties of In_2Se_3, the device achieves an extended retention time of post-synaptic current (PSC) and enhanced device performance in terms of responsivity (R) and detectivity (D) over $PdSe_2$-based counterparts.

View Article Online
DOI: 10.1039/D5MH02349A

Data availability -

The data supporting this article have been included as part of the Supplementary Information.

View Article Online
DOI: 10.1039/D5MH02349A

Optically controlled synaptic device based on $PdSe_2$ / α-In_2Se_3 vdW heterostructure FET

Anurag Ghosh, Inbar Dahan, Bisweswar Santra, Gautham Vijayan, Michael Uzhansky and Elad Koren*

Nanoscale Electronic Materials and Devices Laboratory, Faculty of Materials Science and Engineering, Technion - Israel Institute of Technology, Haifa 3200003, Israel.

**eladk@technion.ac.il*

Abstract

Visual synaptic devices hold great promise for advanced neuromorphic hardware, offering a viable solution to the von Neumann bottleneck. Yet, achieving bidirectional optical control remains a considerable challenge. Herein, we demonstrate an all 2D heterostructure FET consisting of few-layer $PdSe_2$ and α-In_2Se_3, designed as an optically controlled synaptic device with ferroelectric assisted tunability. The device emulates multiple forms of spike-dependent plasticity, exhibiting excitatory and inhibitory synaptic responses in 642–980 nm and 406–520 nm spectral range, respectively. Moreover, the optically induced excitatory and inhibitory synapse can be modulated by electrical gate pulse, utilizing the spontaneous polarization of α-In_2Se_3. By leveraging the coupled ferroelectric and optical properties of In_2Se_3, the device achieves an extended retention time of post-synaptic current (PSC) and enhanced device performance in terms of responsivity (R) and detectivity (D) over $PdSe_2$-based counterparts. Logic gate operations (OR and AND) were demonstrated using 642 nm, 785 nm and 406 nm wavelengths as optical inputs. In addition, three-layer artificial neural network (ANN) was trained to recognize 28×28 pixels handwritten MNIST dataset by backpropagation algorithm demonstrating high recognition accuracy of 96% and 97% under 642 nm and 406 nm, respectively. This study provides an effective strategy for the development of versatile optically controlled neuromorphic devices as fundamental building blocks for on-chip optical communication, optoelectronic logic, and Internet of Things (IoT) applications.

Introduction

In recent years, substantial advancements in artificial intelligence (AI) have led to a growing demand for high-speed, low-power computational systems. The conventional von Neuman computing architecture faces inherent limitation to fulfil these requirements due to its segregated design of the data receiver, processor, and memory units. This separation not only introduces latency but also exacerbates power consumption, posing challenges for next generation AI, big data, and IoT.[1–3] On the other hand, functional diversification at single device level has become essential to continue the downscaling trend in the era of 'More than Moore'.[4] In recent years, extensive research has been focused on the development of neuromorphic based devices, with particular emphasis on visual synaptic operation to emulate human visual perception, memory, and logic at the single-device level.[5,6]

In the human neural system, sensory stimuli comes from the external world through various inputs such as vision, hearing, and smell, with the majority of ~ 80% being received through

View Article Online
DOI: 10.1039/D5MH02349A

visual perception.[7,8] Similarly, artificial visual synapses have the potential to play a dominant role in sensory processing such as image recognition, smart detection and adaptation in real time with minimal power consumption.[3] Yet, most of the reported visual synaptic devices involve hybrid manipulation approaches with both optical and electrical stimuli, introducing similar challenges such as operational complexity, computational latency and high-power consumption, due to bandwidth-connection density trade-off.[2,5,9–16] For example, Wang *et al.* demonstrated a retina-like vision sensor based on van der Waals (vdW) heterostructure (HS) field-effect transistor (FET); where, a continuous gate bias was required to obtain a negative photoresponse for bipolar cell like functionality, which complicates the device operation.[5] Conventionally, optical stimulation is associated with potentiation, representing the learning process, while electrical stimulation is linked to depression, corresponding to the forgetting process.[14,17,18] Inspired by the neural system from human retina, fully optical controlled synaptic device can overcome these challenges providing high bandwidth, low crosstalk, ultralow power consumption and simplified hardware design.[3,18–20] Such optically modulated synapse relies on positive photoconductivity (PPC) and negative photoconductivity (NPC) for potentiation and depression, respectively.[21] Recently, heterostructures composed of different non-layered materials as well as the integration of 2D materials with conventional bulk materials have been employed to realize all-optically controlled visual synapses such as IGZO/SnO/SnS, ZnAlSnO/SnO, perovskite/ZnO etc.[3,18,20,22,23]

Moreover, several studies have explored optically controlled visual synapses solely based on vdW materials, which can further utilize their exceptional optoelectronic properties and dangling-bond-free surfaces for advancing the downscaling trend in modern electronics.[2,4,24–29] In this regard, $PdSe_2$ has garnered significant attention due to its wavelength-dependent bidirectional photoresponse, high carrier mobility of 40,000 cm^{-2} $V^{-1}s^{-1}$, thickness-dependent bandgap (ranging from 1.3 eV for monolayer to 0.03 eV for bulk), and excellent air stability,[27,30] making it particularly advantageous for low power broadband photodetection applications across the UV to IR spectrum.[27,31] The reported synaptic operation in these devices primarily explained either through charge trapping mechanism at the interface between the channel and substrate or via slow carrier recombination facilitated by oxidation-induced localized traps at the channel surface. Hence, the PSC exhibits volatile characteristics due to limited trapping strength and significant variability due to altered interfacial charactersitics.[26,27,32,33] In contrast, non-volatile synaptic memristors provide an excellent platform for maintaining long-term synaptic weights.[34] In particular, coupling interfacial trapped charges with ferroelectricity can significantly extend the retention time of PSC levels and enhance the functionality and performance of 2D based neuromorphic devices.[32,33,35] In this regard, α-In_2Se_3 has emerged as a promising material for neuromorphic applications, primarily due to its unique ferroelectric properties.[9,12,36–38] It exhibits room-temperature, intercoupled in plane (IP) and out of plane (OOP) ferroelectricity down to the monolayer limit alongside excellent optical properties.[39,40] In particular, its remanent polarization enables non-volatile memory (NVM) characteristics without requiring a continuous applied voltage,[41,42] where its direct bandgap and efficient light absorption, make it a suitable platform for multibit optical random access memory (O-RAM), in-memory sensing and logic applications utilized by streamlined read-write operations via a combination of optical and electrical pulses.[2,43]

Herein, we have integrated few layers semiconducting $PdSe_2$ and ferroelectric In_2Se_3 to realize a bidirectionally optical controlled 2D synaptic device with ferroelectric assisted tunability. In this heterostructure, $PdSe_2$ serves as the FET channel, while In_2Se_3 acts as the virtual gate medium through dipole arrangements, modulating both the conducting state and photoresponse. In particular, the device demonstrates excitatory postsynaptic current (EPSC) and inhibitory postsynaptic current (IPSC) under illumination with 642–980 nm and 406–520 nm wavelengths, respectively. The device can effectively replicate all kinds of synaptic plasticity such as spike-duration-dependent plasticity (SDDP), spike-number-dependent plasticity (SNDP), spike-rate-dependent plasticity (SRDP), and intensity-dependent plasticity for both potentiation and inhibition. The EPSC at longer wavelengths arises from the PPC effect of both $PdSe_2$ and In_2Se_3, with In_2Se_3 predominantly generating electron-hole pairs due to its direct bandgap nature. Conversely, the IPSC is attributed to NPC behaviour of $PdSe_2$, stemming from oxygen desorption and light-induced defect states under shorter wavelengths.[27,44] Moreover, intense 406 nm light can be employed to use the device in reconfigurable manner by enabling a rapid RESET process. As a result, the device can be implemented and reconfigured for basic logic gate operations such as 'OR' and 'AND' solely by using visible light as input signals. In addition, the optically induced EPSC and IPSC can be further modulated with electrical gate pulse leveraging the ferroelectric property of In_2Se_3. Based on the device characteristics, a simulation-based ANN was utilized to process 28 × 28 pixels handwritten dataset by backpropagation algorithm demonstrating high recognition accuracy of 96% for 642 nm and 97% for 406 nm. The presented vdW HS device enables precise modulation of synaptic response by pulse amplitude, duration, and frequency of both optical and electrical signals, showcasing a promising platform for neuromorphic and optoelectronic applications.

Results and Discussion

Device structure and characterization

In biological systems, neural networks consist of a vast array of hierarchically organized interconnected neurons communicating through synapses (Figure 1a).[21] Depending on the input stimuli, pre-synaptic membrane releases different types of neurotransmitters that results in either EPSC or IPSC. An equivalent artificial synapse can be realized using a three-terminal FET architecture, where the channel functions as the synapse, and the channel current (I_D) represents the PSC. Presynaptic signals can be applied in the form of optical or electrical pulses. In our fabricated system the gate terminal was used as modulatory input to regulate or attenuate the EPSC and IPSC induced by optical pulses.

To realize an optically controlled synaptic behaviour with an additional degree of freedom to modulate the optical synapse by gate actuation, an artificial synaptic FET is proposed based on In_2Se_3 - $PdSe_2$ heterostructure (Figure 1b). α-In_2Se_3 was exfoliated by conventional scotch tape method on a prepatterned conductive Si substrate coated with 300 nm thick SiO_2. Few-layer $PdSe_2$ was exfoliated onto a PDMS stamp and subsequently transferred onto In_2Se_3 using a dry transfer method (Methods section). To achieve an asymmetric geometry, $PdSe_2$ was partially deposited over α-In_2Se_3,[45,46] enabling a balance between the PPC effect of α-In_2Se_3 and the NPC effect of $PdSe_2$. A comprehensive explanation of this configuration is provided in the Operation Mechanism section. In_2Se_3 was employed as a gate-switching medium, leveraging its ferroelectric properties, while $PdSe_2$ served as FET channel. A global back gate was utilized

View Article Online
DOI: 10.1039/D5MH02349A

for ferroelectric polarization modulation, and light illumination served as the primary input stimulus to regulate the PSC. $PdSe_2$ flakes with a thickness of 10–15 nm and In_2Se_3 flakes with a thickness of 15–20 nm were selected for device fabrication (Figure 1c, d). Raman spectroscopy was conducted to assess the crystalline quality of the 2D flakes prior to the optoelectronic measurements (Figure 1e). The Raman signals were collected from different regions of the device, as indicated in the optical micrograph of the device (Figure 1c). The black spectrum represents pristine $PdSe_2$, exhibiting four characteristic peaks at ~147.1 cm^{-1}, ~ 210.7 cm^{-1}, ~ 226.7 cm^{-1}, and ~ 261 cm^{-1}, which correspond to the A_g^1-B_{1g}^1, A_g^2, B_{1g}^2, and A_g^3 vibrational modes, respectively.[27,31] The red spectrum corresponds to pristine In_2Se_3, which exhibits a sharp characteristic peak at ~106 cm^{-1}, attributable to the A_1 (LO+TO) phonon mode and two additional twin peaks, observed at ~183.4 cm^{-1} and ~199.4 cm^{-1} that are assigned to the A_1 (LO) and A_1 (TO) phonon modes, respectively. The LO-TO splitting of the A_1 mode provides well established evidence of centrosymmetry breaking and the emergence of ferroelectricity in In_2Se_3.[39,42,47] Additional direct evidence of non-volatile ferroelectric switching in α-In_2Se_3 using Piezoelectric microscopy (PFM) measurements are shown in Figure S1 and are in agreement with previous reports.[48–53] The blue spectrum represents the Raman signal from the overlapping region, where all the characteristic peaks of both In_2Se_3 and $PdSe_2$ are observed.

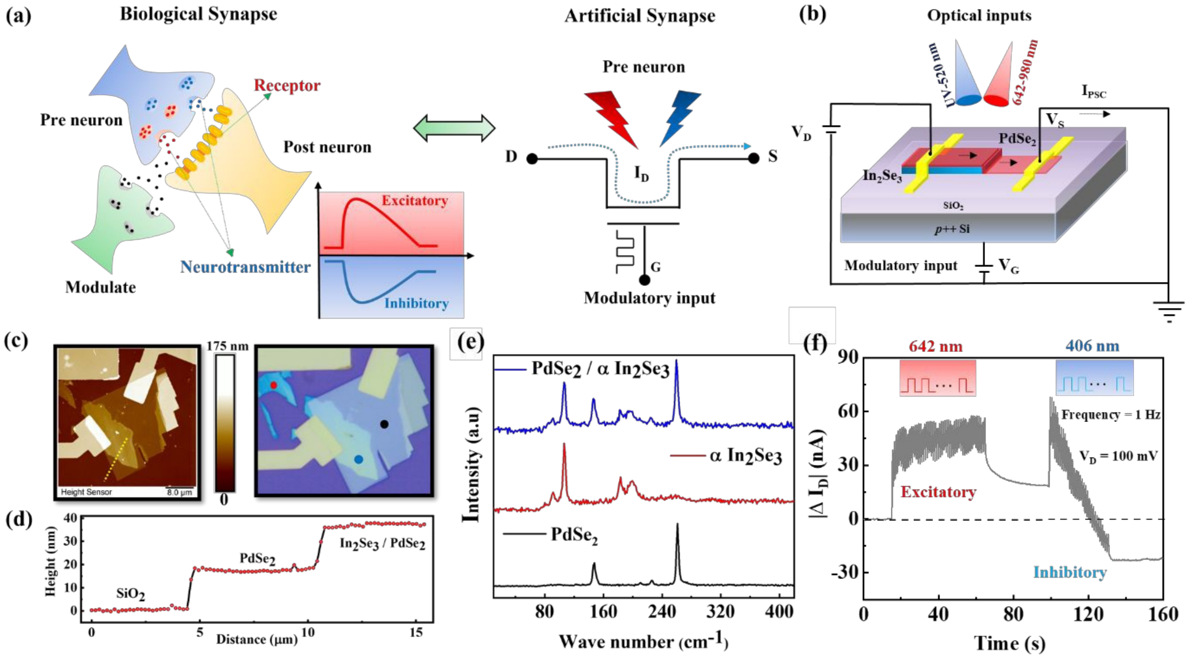

Figure 1: (a) Schematic illustration of biological and artificial synapses. Two types of neurotransmitters determine the firing state of post neuron being either excitatory or inhibitory. The generated EPSC or IPSC can be further controlled by modulatory input. The equivalent artificial synapse of three terminal FET architecture where PSC is primarily generated by optical input and further modulated by gate electrical input. (b) Schematic diagram of $PdSe_2$-In_2Se_3 neuromorphic device. (c) Topographic and optical image of the device. (d) Height profile of $PdSe_2$ and In_2Se_3 flakes. (e) Raman spectra of $PdSe_2$ (black spot in (c)), In_2Se_3 (Red spot) and heterostructure (Blue spot). (f) Temporal photoresponse under successive illumination of 642 nm and 406 nm light pulses. (Frequency = 1 Hz, Pulse width = 0.5 s).

View Article Online
DOI: 10.1039/D5MH02349A

As discussed above, the device exhibits both potentiation (EPSC) and inhibition (IPSC) states using two characteristic wavelengths, 642 nm and 406 nm, respectively without relying on any additional electrical control. Figure 1f illustrates the change in drain current following stimulation by multiple light pulses of 642 nm followed by 406 nm at a frequency of 1 Hz. A low read voltage of 100 mV (V_D) was applied to measure the drain current through the $PdSe_2$ channel. Closer inspection reveals that the device shows an instant PPC under 406 nm illumination, whereas I_D gradually decreases as time of illumination prolonged (Figure S2). Additionally, the device demonstrates IPSC under 520 nm stimulation, although the rate of achieving the depression is milder compared to 406 nm (Figures S3a and S3b). Similarly, the device demonstrates potentiation characteristics under illumination extended up to 980 nm, as $PdSe_2$ is capable of sensing light within the infrared range as well (Figure S3c).

Optically induced Synaptic Plasticity

To demonstrate that the device effectively replicates various forms of spike-dependent plasticity solely through optical stimulation for both potentiation and inhibition, two representative wavelengths of 642 nm and 406 nm were selected. To demonstrate the variation from short-term plasticity (STP) to long-term plasticity (LTP), the device was exposed to 642 nm light illumination for 10 consecutive pulses of different duration with same time interval (Figure 2a). As the pulse duration increases from 10 ms to 500 ms, the PSC level (following the 10th pulse) increased from ~3.5 nA to ~18 nA. A similar behaviour was observed by varying the number of pulses (SNDP) while maintaining the same pulse duration (0.5 s) and frequency (1 Hz) (Figure 2b) and by varying the light intensity (Figure 2c). Figure 2d depicts the modulation from STP to LTP demonstrating SRDP by varying the time interval (Δt) between two consecutive pulses for a time duration of 100 s, while maintaining a constant pulse width of 1 s. In particular, the PSC level decreases from ~26 nA to ~10 nA, as Δt increases from 0.2 s to 25 s. To get further insight about the correlation between memory level and Δt, we have calculated the paired-pulse facilitation (PPF) index, which is a critical parameter used to characterize STP in biological synapses,[18,27] using the following equation:

$$PPF\ index = \frac{A_2}{A_1} \times 100\ \% \tag{1}$$

Here, A_1 and A_2 represent the amplitudes of the photocurrent corresponding to the first and second pulses, respectively, as illustrated in Figure 2e. As shown in Figure 2f, the PPF index exhibits an exponential dependence on Δt, aligning well with the principles of neurobiology.[3] The calculated data was fitted using the following equation:

$$PPF\ index = A_0 + C_1 \times exp\left(-\frac{\Delta t}{\tau_1}\right) + C_2 \times exp\left(-\frac{\Delta t}{\tau_2}\right) \tag{2}$$

Where, C_1 and C_2 represent the initial magnitudes, while τ_1 and τ_2 denote the fast and slow relaxation time constants, respectively. Based on equation (2), the extracted values of τ_1 and τ_2 were found to be 0.5 s and 8.78 s, respectively. Notably, the device achieved a maximum PPF index of 138% at Δt = 0.2 s, demonstrating its decent performance compared to recently reported studies.[3,18]

View Article Online
DOI: 10.1039/D5MH02349A

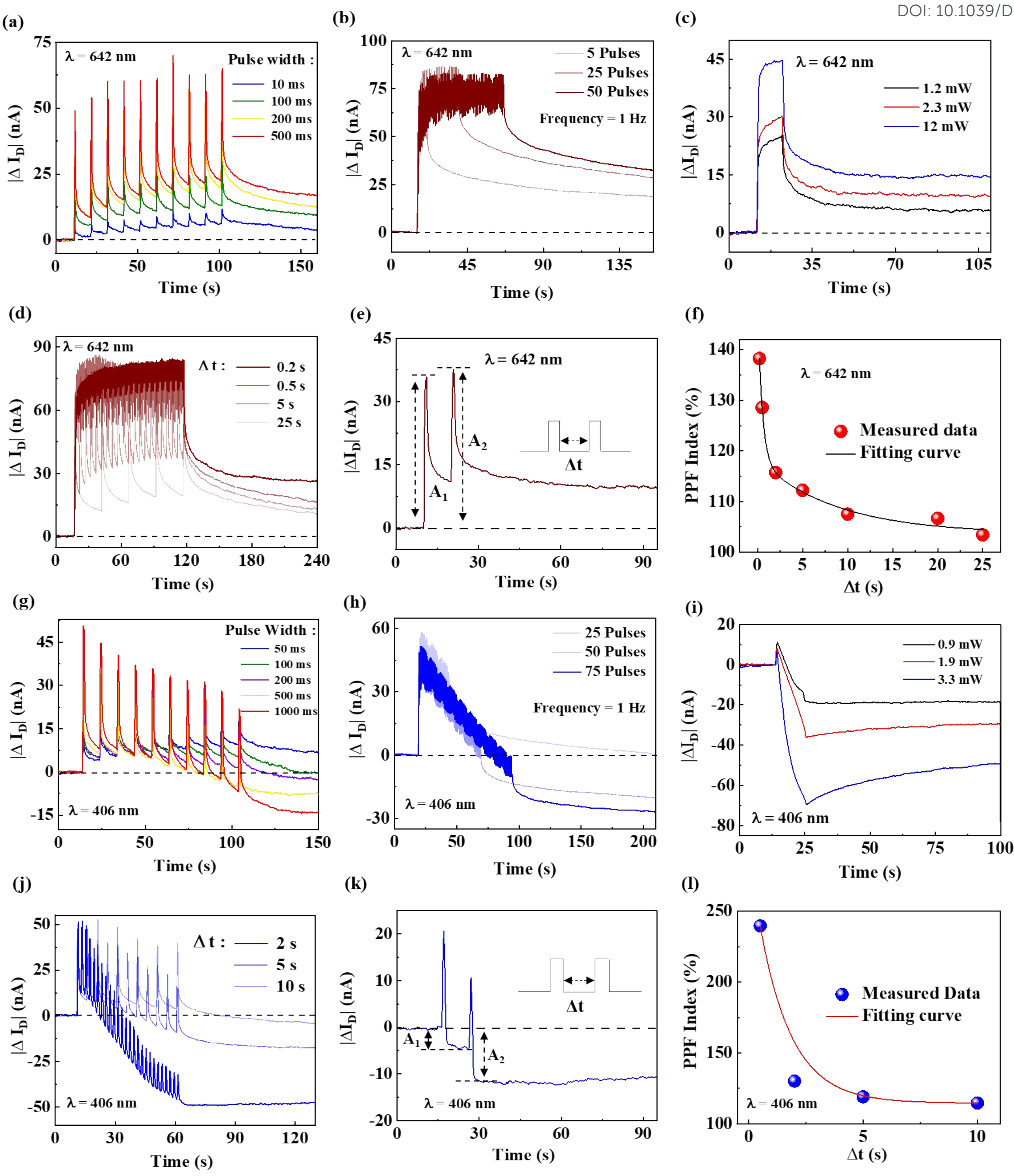

Figure 2: (a) STP to LTP transition by different pulse width of 642 nm light. (b) EPSC triggered by different number of 642 nm light pulses (Pulse width = 0.5 s, Frequency = 1 Hz). (c) EPSC triggered by varying intensities of 642 nm light with a pulse width of 10 s. (d) EPSC triggered by different pulse interval (Δt) of 642 nm light (Pulse duration = 1 s). (e) EPSC stimulated by two consecutive 642 nm light pulses at 10s of interval, where A_1 and A_2 represents the amplitude of photocurrent achieved after 1st and 2nd pulse respectively. (f) PPF index as a function of pulse interval. (g) STD to LTD transition by different pulse width of 406 nm light. (h) IPSC triggered by different number of 406 nm light pulses. (Pulse width = 0.5 s, Frequency = 1 Hz). (i) IPSC stimulated by different intensities of 406 nm light with pulse width of 10s. (j) STD to LTD transition by different pulse interval of 406 nm light. (k) IPSC stimulated by two consecutive 406 nm light pulses at 10 s of interval, (l) PPF index as a function of pulse interval.

View Article Online
DOI: 10.1039/D5MH02349A

Analogous forms of synaptic plasticity associated with inhibitory responses were successfully demonstrated, as shown in Figures 2g-2l, indicating that the transition from short term depression (STD) to long term depression (LTD) can be achieved through 406 nm excitation. Notably, Figure 2g, that illustrates SDDP, highlights the intriguing interplay between PPC and NPC under 406 nm exposure, where for the shortest pulse durations (50 ms), the device exhibits a small potentiation trend driven by the PPC effect. However, as the pulse duration increases, the NPC effect becomes dominant, leading to depression state. This behaviour underscores the dynamic competition between two opposing photoconductive effects governing the synaptic response. Similarly, the PPF index associated with the inhibitory process under 406 nm stimulation is presented in Figure 2h, where τ_1 and τ_2 are calculated to be 1.12 s and 1.36 s, respectively. These results emphasize the device versatility in emulating complex synaptic behaviours by using two representative wavelengths. Although bidirectional synaptic plasticity can be realized without the application of an external gate voltage, the polarization state of In_2Se_3 can be deterministically programmed by applying a gate-voltage pulse prior to optical stimulation enabling further tunability of the synaptic response, as discussed in the following section.

Polarization dependent Optical synapse

The optically induced synaptic plasticity of the $PdSe_2$-In_2Se_3 device can be further modulated through electrical gate pulses, harnessed by the ferroelectric properties of In_2Se_3. Electric polarization dependant measurements were conducted for both 406 and 642 nm wavelengths following different gate induced poling conditions. In the first step, an electrical gate pulse of different amplitude and polarity was applied to align the dipoles in In_2Se_3. Following the poling process, a 2 min delay time was obtained before performing the I_D-t measurements with light pulses to minimize gate-induced trapping effects (Figure S4a & S4b). Subsequently, the device was subjected to a series of light pulses at an interval of 10 s with a duration of 1 s. As shown in Figure 3a, the photocurrent for 642 nm light illumination increases with the transition of gate poling conditions from negative to positive, resulting in higher PSC levels. Figure 3b demonstrates the progressive increase in photocurrent for the 1st and 10th light pulses, rising from 19.8 nA to 50 nA and 23 nA to 62 nA, respectively as poling condition changes from $-V_G$ to $+V_G$, resulting in enhanced EPSC. Additionally, the difference in photocurrent between the 1st and 10th pulse grows with positive gate voltage, corroborating the observation that under distinct poling conditions, the photocurrent requires different time to reach saturation level. This demonstrates the capability to achieve distinct current levels for LTP, independent of pulse duration and frequency. Furthermore, the PPF function shows a clear linear dependence on the gate poling conditions for an identical input stimulus (Figure S4c), enabling to control the potentiation level by applying an electrical gate pulse beforehand. Such linear behavior of the PPF was observed across all measured devices. The EPSC following two opposite poling conditions of ± 90 V with various frequencies of light pulses are presented in Figure S5, confirming that the variable current level for LTP can be effectively established by introducing an electrical gate pulse.

Similar gate modulation was observed associated with IPSC under 406 nm exposure (Figure 3c and Figure S5f). In particular, a distinct level of LTD ranging from -3 nA to -15.6 nA is obtained depending on the gate induced poling conditions. It is important to note that for the IPSC (EPSC) measurements, the PSC levels following negative (positive) gate poling are rather closely spaced in comparison with those obtained following positive (negative) gate actuation.

View Article Online
DOI: 10.1039/D5MH02349A

This can be clearly seen in the representative figures showing that the adjacent profiles representing opposite gate polarities are rather closely spaced. Therefore, for better visualization, we have included few representative profiles to show the effect of modulation. Complete datasets with uniform gate intervals are provided in Figure S6. The device exhibits the highest levels of both IPSC and EPSC under positive poling attributed to the strongest photoresponse due to the dipole-induced band alignment of the heterostructure device (see further discussion below). As mentioned above, there is a competition between PPC and NPC during the inhibition process, which is clearly observable in Figure 3d. Although the photoresponse for both the 1st and 10th light pulses increases with positive gate poling, the photoresponse of the 10th pulse is lower than that of the 1st pulse for each poling condition. This indicates that the NPC effect from $PdSe_2$ becomes increasingly dominant with time until overcoming the PPC effect from In_2Se_3.

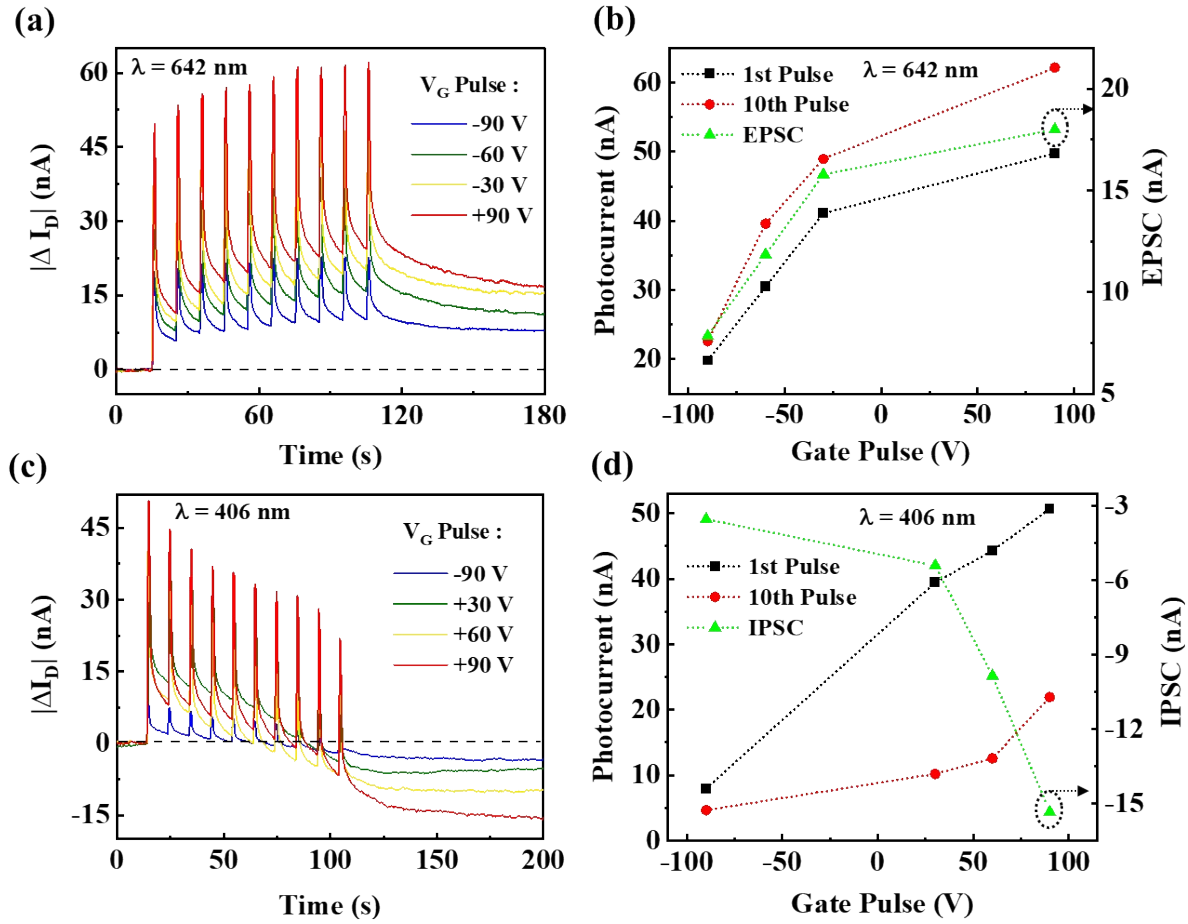

Figure 3: (a) Gate modulation of synaptic plasticity under 642 nm excitation (Pulse duration = 1 s, Frequency 0.1 Hz). (b) Photoresponse measured (under 642 nm) after 1st and 10th light pulses and EPSC measured after 10th pulse with respect to gate actuation. (c) Gate modulation of synaptic plasticity under 406 nm excitation. (d) Photoresponse measured (under 406 nm) after 1st and 10th light pulses and IPSC measured after 10th pulse with respect to gate actuation.

View Article Online
DOI: 10.1039/D5MH02349A

The presence of In_2Se_3 significantly enhances the overall photoresponse of the device and its intrinsic ferroelectric field plays a key role in sustaining the PSC levels over extended periods. This behaviour was confirmed by comparing between the I_D-t measurements (Figure S7a-c) conducted under 642 nm and 406 nm pulses for $PdSe_2$ and the HSFET. The enhanced photoresponse behaviour (under 642 nm illumination) is further supported by the calculated responsivity (R) and detectivity (D) values of the $PdSe_2$ and the HS FET (Figure S7a). In particular, the responsivity is measured to be 2.11 A/W for the HS FET and 0.07 A/W for $PdSe_2$ FET. The nearly 30 times increase in responsivity in the HS FET is attributed to the direct bandgap nature of In_2Se_3, which enables superior photon absorption compared to the indirect bandgap of $PdSe_2$.

Detectivity was found to be 0.75×10^{10} Jones for the HS FET and 0.87×10^{8} Jones for the $PdSe_2$ FET, demonstrating that the integration of In_2Se_3 enhances detectivity by nearly two orders of magnitude. It is also important to note that the presented current levels are device specific due to geometry variations of the FET channel area and heterojunction overlap between the In_2Se_3 and the $PdSe_2$ components. All calculated parameters correspond to measurements, that were performed at a drain bias of 100 mV.

Operation Mechanism

To understand the bidirectional photoresponse of the device, I_D-V_G measurements were performed in dark and illuminated conditions. As shown in Figure 4a, the transfer curve consists of a hysteretic loop attributed to both ferroelectric dipole switching and trapping -de trapping process at the In_2Se_3-$PdSe_2$ interface. Our discussion focuses on the photoresponse at $V_G = 0$ V as the operational condition relevant for synaptic measurements corresponding to the shaded region in Figure 4a (magnified in Figure 4b). The device demonstrates an increase in conductivity under 642 nm light illumination in both sweep directions, indicative of usual positive photoconductive behaviour, in agreement with the observed synaptic response. The magnified view shown in Figure 4b highlights that the photoresponse following negative poling (forward sweep) is slightly lower than that following positive poling (backward sweep, marked as regions I and II), consistent with the polarization dependent photoresponse results. The PPC effect observed under 642 nm illumination is attributed to both In_2Se_3 and $PdSe_2$, as both materials absorb this wavelength. In particular, photogenerated charges that are absorbed in the In_2Se_3 can transfer to the $PdSe_2$ channel enhancing the overall photoresponse of the device.

View Article Online
DOI: 10.1039/D5MH02349A

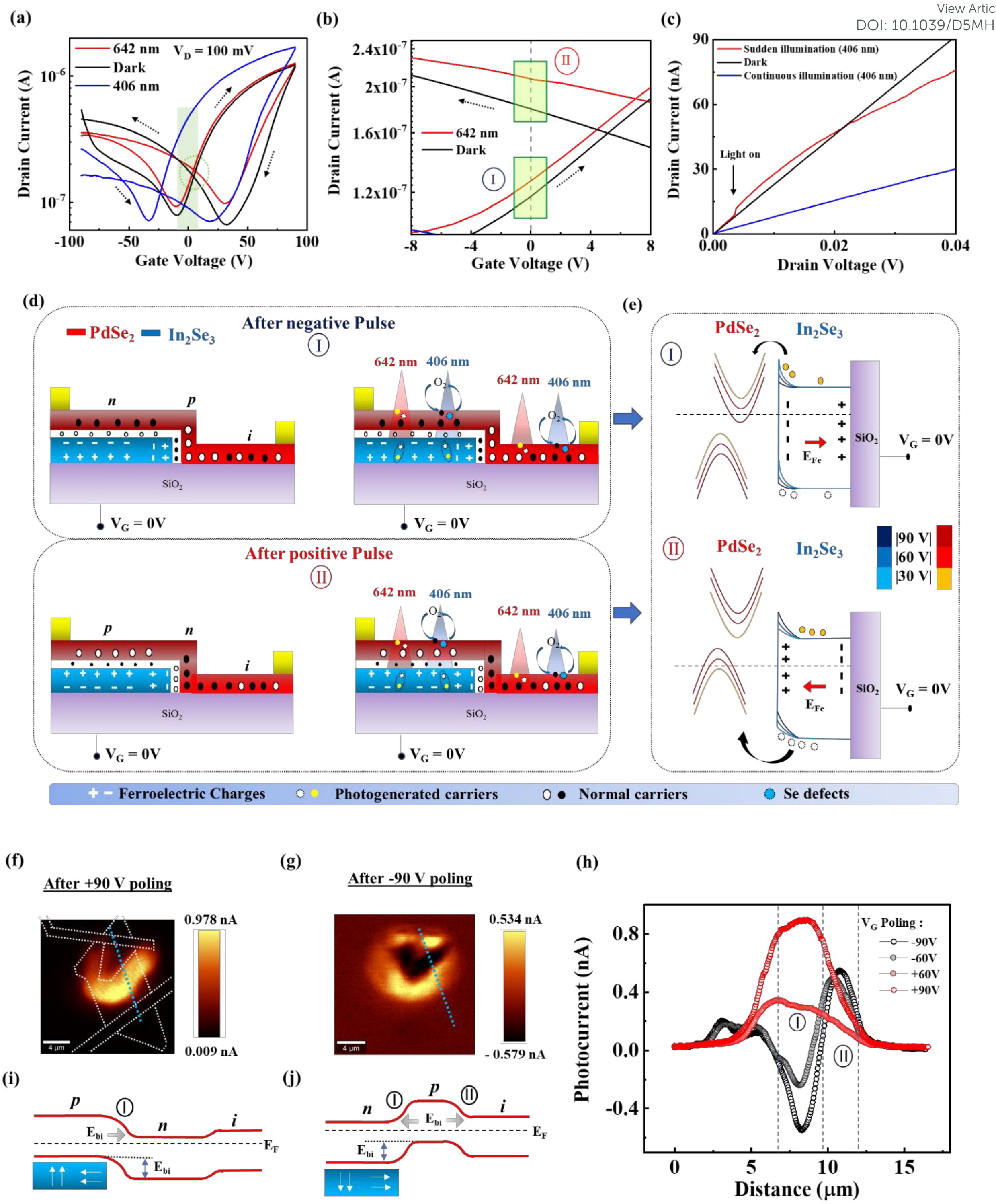

Figure 4: (a) Transfer characteristic curve in dark and under light illumination (V_D = 100 mV). (b) Enlarged figure of the circle area in figure (a). (c) I_D - V_D curve of the device measured under dark, continues and sudden 406 nm light illumination. Sudden illumination results in instant PPC but gradually transit to NPC. (d) Schematic representation of channel conducting state and dipole arrangement following negative (I) and positive (II) gate actuations in dark (left) and light (right) for 642 nm and 406 nm. (e) Energy band diagram of the $PdSe_2$-In_2Se_3 HS interface and charge transfer characteristics of photogenerated carriers following negative (top) and positive (bottom) gate actuations. Solid circles refer to electrons and hollow circles refers to holes. Photocurrent mapping of

View Article Online
DOI: 10.1039/D5MH02349A

the device following (f) +90V gate poling, (g) -90V gate poling. (h) Line profiles of the photocurrent along the blue dotted lines in (f) and (g) following ±90V and ±60V gate poling. Energy band diagrams of $PdSe_2$ channel following (i) +90V gate poling, (j) -90V gate poling. Red lines refer to the conduction and valance bands of $PdSe_2$. White arrows in the blue shaded box depicts the OOP and IP dipole orientation in In_2Se_3.

The transfer characteristics were also measured under 406 nm light illumination (blue curve in Figure 4a) to consider the IPSC**,** where a clear light-induced doping effect is evident, manifested by a leftward shift of the I_D-V_G curve with respect to dark conditions. Such *n*-type doping effect causes an unusual NPC effect in the $PdSe_2$ channel. Previous studies have reported that $PdSe_2$ exhibits NPC under shorter visible wavelengths illumination by light-induced defect states, resulting in oxygen desorption from its surface.[27,44,54] In particular, 406 nm light illumination causes oxygen adatoms to be ejected from the surface, leaving behind electron, resulting in *n*-type doping effect (Figure S8). Similarly, high energy photons of short wavelength create Se vacancy sites, introducing shallow electronic trapping states near the conduction band, resulting in *n*-type device characteristics.[27,44] Recent experiment and theoretical studies validated the effect of environmental oxygen pressure on this NPC effect in $PdSe_2$ as well as in $PtSe_2$ and $PtTe_2$.[55–57] The degree of doping level with varying light intensity is presented in Figure S9. I_D-V_D measurements in Figure 4c further reveal that 406 nm light stimulation induces an instant PPC, mainly attributed to carrier generation in the underlying In_2Se_3. As time progresses, the current decreases below the dark current level, indicating the dominance of the NPC effect from $PdSe_2$. In comparison, a fully symmetric HS device in which $PdSe_2$ is completely supported by In_2Se_3 presents a minor leftward shift in transfer curve under continuous 406 nm light illumination (Figure S10a), due to the dominant PPC effect by the In_2Se_3. Therefore, by strategically designing a partially covered In_2Se_3 layer by $PdSe_2$ device, the two opposing photoconductive effects are jointly present, achieving both EPSC and IPSC by optical stimulation.

To interpret the polarization dependent photoresponse and the underlying charge transfer across the In_2Se_3 - $PdSe_2$ interface, device configurations for opposite poling conditions under dark and illuminated states are schematically presented in Figure 4d. Following negative gate poling, the OOP electric dipoles arrange such that they point away from the $PdSe_2$ side, leading to positive holes trapping at the interface between $PdSe_2$ and In_2Se_3 and *n*-type channel characteristics. Conversely, following positive poling, *p*-type channel characteristics are introduced. The I_D-V_G curve of the symmetric HS FET similarly confirms that $PdSe_2$, shifts from *n*- type ambipolarity to *p*-type ambipolarity following two opposite poling conditions, due to the ferroelectric polarization within the underlying In_2Se_3 (Figure S10). In addition, in the case of an asymmetric HS FET, the intercoupled IP dipoles form hole (electron) region in $PdSe_2$ next to the edge of In_2Se_3 following negative (positive) poling (see sections below).[39,45,46] Kelvin probe force microscopy (KPFM) was used to determine the relative energy band positions of In_2Se_3 and $PdSe_2$ (Figure S11). In particular, the Fermi level of In_2Se_3 lies 0.39 eV above Au, while that of $PdSe_2$ is 0.251 eV below In_2Se_3. These relative Fermi level positions in the pristine state are consistent with previous reports based on UPS, KPFM, and theoretical studies.[58–60]

Based on the measured surface potential characteristics of the In_2Se_3-$PdSe_2$ heterojunction, energy band diagrams of the In_2Se_3-$PdSe_2$ interface are depicted in Figure 4e, where blue and

View Article Online
DOI: 10.1039/D5MH02349A

red shaded lines denote the bands structure of In_2Se_3 and $PdSe_2$, respectively, following different gate-induced ferroelectric polarization. For negative poling, the energy bands of $PdSe_2$ bend downward. As a result, the conduction band of $PdSe_2$ shifts closer to the Fermi level as it forms *n*-type channel (as evident by the I_D-V_G profiles of the symmetric HS). Since the work function of $PdSe_2$ is higher than that of In_2Se_3, the energy bands of In_2Se_3 bend upwards, creating a built-in potential at the interface.[59] Under illumination, photogenerated electrons from the In_2Se_3 layer cannot efficiently transfer to the $PdSe_2$ channel due to this potential barrier, resulting in a reduced photoresponse. In contrast, following positive gate poling, the energy bands of $PdSe_2$ bends upward and the valance band become close to the Fermi level. Since the FET channel is now formed by holes, photogenerated holes can favourably move across the In_2Se_3 - $PdSe_2$ interface leading to higher photoresponse compared to the negative poling condition.

Depending on the gate poling history, photogenerated charges (*e* or *h*), become confined at the interface due to the OOP of In_2Se_3. This attractive field stabilizes the trapped charges for an extended period acting as a virtual gate voltage resulting in longer PSC in HS FET. In contrast, in pristine $PdSe_2$ FET, light-induced trapped charges at the $PdSe_2$-SiO_2 interface rapidly decay resulting in the absence of PSC due to the lack of a dipolar field. The role of dipolar field in sustaining the PSC level is further verified by measuring I_D-t in both symmetric and asymmetric HS FET (Figure S7d).

To experimentally validate the above-mentioned device electronic configuration, scanning photocurrent microscopy (SPCM) was performed following different poling conditions (Figure 4f-h & Figure S12). During the measurements, the drain bias was kept at 0 V to directly probe the ferroelectrically induced lateral built in electric fields formed across the $PdSe_2$ channel. A 532 nm laser with an incident power of ~ 0.3 mW was used to scan the device area. The device geometry is outlined by the white lines in Figure 4f, and the corresponding optical micrograph and scanned area are presented in Figure S13a.

Photocurrent maps following +90V and -90V poling are shown in Figures 4f and 4g, respectively. Figure 4h shows the corresponding line profiles along the blue dotted path drawn in Figure 4f and 4g, where the red and black traces represent positive and negative poling states, respectively. Following positive poling, a positive photocurrent peak is observed next to the In_2Se_3 edge (region I), whereas following negative poling, the photocurrent reverses its direction in region (I) and an additional positive peak emerges few microns away from the In_2Se_3 edge (region II). This photocurrent polarity modulation directly stems from the reversal of both IP and OOP ferroelectric dipoles within the underlying In_2Se_3. In particular, under positive poling, OOP dipoles induce a *p*-type channel within the overlapping HS region, whereas IP dipoles give rise to localized *n*-type doping in $PdSe_2$ next to the In_2Se_3 edge (region I), forming a *p–n* junction (Figure 4i). Given that the native $PdSe_2$ is slightly *n*-type (Figure S13b), the influence of IP dipoles can extend further into the $PdSe_2$ channel. Conversely, following negative poling and dipole reversal, an *n–p* junction is formed and the photocurrent becomes negative (region I in Figure 4j). Meanwhile, IP dipoles accumulate holes over a limited range, resulting in the formation of a secondary *p–i* junction at region (II), forming a positive photocurrent peak. The observed modulations in the built in electric fields across the $PdSe_2$ channel confirm the reversal of ferroelectric dipole configuration following alternating gate actuations. Moreover, the evolution of photocurrent amplitude with varying gate-poling voltages (photocurrent map for ±60 V gate poling condition are shown in Figure S13c and S13d, respectively.) is consistent with the device conductive state for different gate voltage

View Article Online
DOI: 10.1039/D5MH02349A

sweep ranges, as shown in Figure S13e and S13f. Figure S13b shows negligible hysteresis in the $PdSe_2$ FET, confirming the absence of a non-volatile electrostatic gating effect at the $PdSe_2/SiO_2$ interface. Moreover, the I_D–t characteristics measured after opposite gate actuations (±90 V) under 642 nm illumination exhibit no significant current variations, indicating that the non-volatile electrostatic gating originates exclusively from the heterostructure region due to dipole switching within the In_2Se_3 (Figure S14). It is important to note that the electrical measurements of the asymmetric heterostructure were conducted at a low drain voltage (V_D) of 100 mV, where negligible non-linear junction characteristics were observed. However, at higher drain voltages, the device exhibits a mild rectifying behavior due to junctions formation (Figure S15) indicating that the polarity of the high drain bias (+/-1V) can affect the overall carrier modulation across the device.[45] Similar electrical and optical characteristics has been seen in other devices (Figure S16) demonstrating the reproducibility of our results.

Binary Logic Operation and Image Recognition

A primary objective of a bidirectional optical synaptic device is to enable SET/RESET operations solely through light stimulation, ensuring a reconfigurable functionality without the reliance on continuous electrical control. Furthermore, integrating Boolean logic operations into such optically controlled synaptic device would offer significant advantages, particularly for on-chip optical communication and photonic integrated circuits.[20,61] In this section, we demonstrate that the In_2Se_3-$PdSe_2$ synaptic device can be rapidly RESET using high-intensity (> 0.17 mW/mm^2) 406 nm light, exploiting the NPC effect of $PdSe_2$ at this wavelength, where the ferroelectric nature of In_2Se_3 enables to retain IPSC for an extended period of time after light illumination. Hence, a 642 nm light pulse can be employed for optical write operations, while 406 nm light enables to perform the optical erase operation. Figure 5a illustrates reconfigurable synaptic operations through optical write and optical erase cycles. Measurements were carried out using a sequence of light pulses from both wavelengths, with no prior application of any poling condition, thereby keeping In_2Se_3 in its natively poled state. It is evident that the transistor "on" state can be effectively switched off within 5 seconds by the application of 406 nm light, demonstrating optical reset capability of the device. Next, two fundamental logic functions i.e., ‘OR’ and ‘AND’ are demonstrated by exploiting the bidirectional photoresponse of this device. Figure 5b illustrates the experimental concept, where two wavelengths 642 nm and 785 nm, serve as inputs A and B, respectively. Additionally, 406 nm light is employed as a modulatory input to switch the operation from OR to AND. In the input logic scheme, the presence of light is designated as logic "1", whereas the absence of light corresponds to logic "0". For the output logic, a threshold current of 0.55 µA was defined, such that output currents exceeding this threshold are classified as logic "1", while currents below the threshold are classified as logic "0." The output current was measured under a drain bias of 100 mV. As observed in Figure 5b, when either input A (642 nm) or input B (785 nm) are on (representing 10 or 01 state), the output current exceeds the threshold value, resulting in an output logic of "1". Conversely, when both light inputs are off (00 state), the output current remains below the threshold, yielding an output logic of "0". This behaviour aligns with the truth table of an OR gate. Subsequently, a 406 nm light pulse was applied to reduce the initial current level, enabling the implementation of an AND gate operation. It can be observed that while only one of the inputs, A or B, is active, the output current does not reach the threshold value, whereas when both inputs, A and B, are active (11 state), threshold is exceeded and thus representing the functionality of an AND gate. Similarly, NOR and

View Article Online
DOI: 10.1039/D5MH02349A

NAND gate logic operations can be potentially realized by increasing the initial current level (above 0.55 uA as state ‘1’) using 642 nm laser illumination and then utilize 406 nm and 520 nm as inputs A and input B.

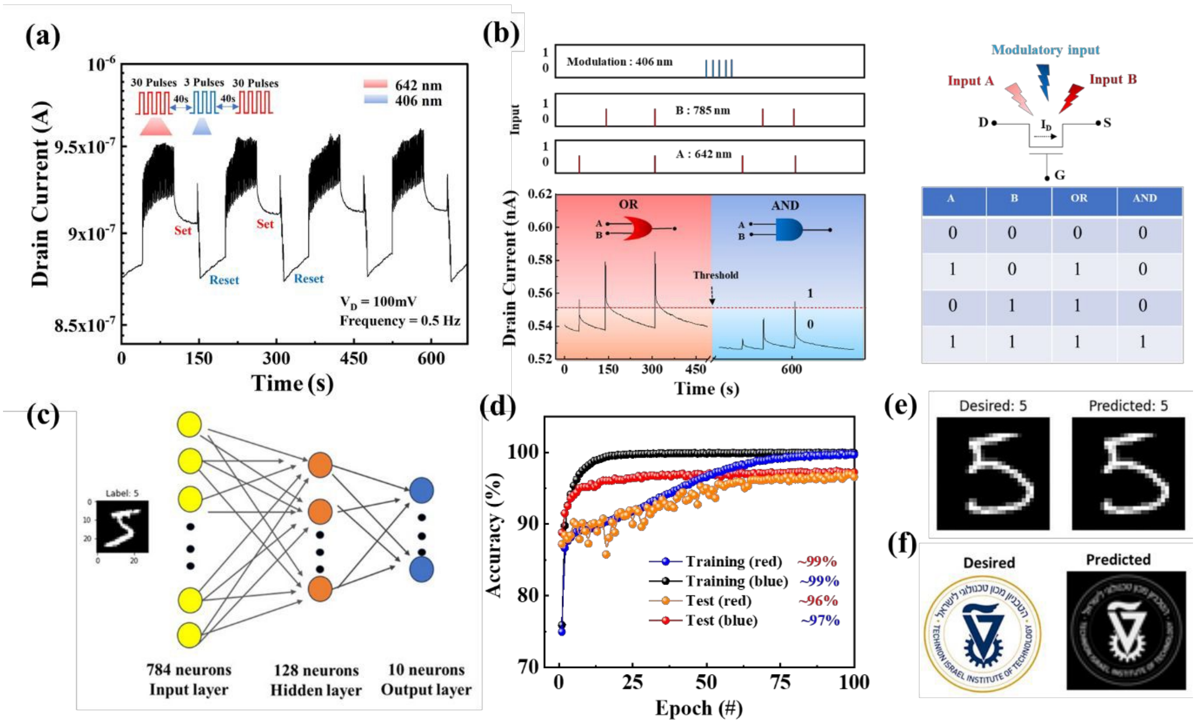

Figure 5: (a) Optical write & optical erase functionalities with 642 nm and 406 nm light pulses (Frequency = 1 Hz) in unpoled $PdSe_2$-In_2Se_3 HS device. (b) Boolean logic gates operations (OR & AND) with 642 nm and 785 nm as two input signals and 406 nm as modulatory input (V_D = 100 mV). (c) Schematic diagram of a three-layer artificial neural network used for simulation of MNIST handwritten digit recognition, (d) The training and test accuracies as a function of the epoch of 28×28 pixels handwritten digit images for with red (642 nm) and blue (406 nm) light pulses of 1 Hz frequencies. (e)-(f) The desired and predicted “5’ of MNIST training data set and arbitrary images using a three-layer ANN, respectively.

Finally, the experimentally observed conductance variations for LTP and LTD (Figure S17) have been directly implemented by a software based artificial neural network (ANN) to perform neuromorphic simulations. For this purpose, a three-layer ANN has been constructed, consisting of an input layer (784 neurons), a hidden layer (128 neurons), and an output layer with 10 neurons representing the class of digits ‘0’–‘9’ (Figure 5c). The hidden layer plays a key role in determining the network performance, as it contains activation functions that process the nonlinear behavior within the ANN. Rectified Linear Units (ReLU) were used as activation functions for the hidden layer, while the ‘Adam’ optimizer was employed for training the output layer. A ‘sparse categorical cross-entropy’ loss function was used as the objective function (Supporting Information).[62] For neuromorphic simulation, the Modified National Institute of Standards and Technology (MNIST) handwritten digit database was utilized, containing 60,000 grayscale images for training and 10,000 for testing and validation. Figure 5d presents the training and test accuracies as a function of training epochs. As shown in Figure 5d and Table S1, the device achieves excellent classification performance for both

View Article Online
DOI: 10.1039/D5MH02349A

red (642 nm, 1 Hz) and blue (406 nm, 1 Hz) lights driven device parameters, demonstrating its ability to emulate a bidirectionally optical controlled artificial synaptic system for neuromorphic hardware applications. Interestingly, blue-light-driven recognition achieves its maximum accuracy with fewer epochs than the red-light case (Table S1). This behaviour can be attributed to the experimentally observed conductance response under blue light, which exhibits smaller variations and a more linear modulation behaviour. Finally, the artificial neural network was employed for image recognition, with the desired and predicted images of the digit "5" from the MNIST dataset (Figure 5e) and for an additional arbitrary image (Figure 5f), exhibiting near-identical features.

Summary

In summary, we demonstrate a bidirectional optical synapse with ferroelectric assisted tunability based on vdW HS FET, by partially overlapping $PdSe_2$ on top of ferroelectric In_2Se_3. The device effectively emulates all forms of synaptic plasticity using visible light. Excitatory synaptic behaviour was achieved under illumination at 642 nm, 785 nm, and 980 nm, while inhibitory synaptic behaviour was observed for 520 nm and 406 nm wavelengths. $PdSe_2$ primarily enables to achieve optically induced IPSC owing to oxygen desorption from its surface under 406 nm and 520 nm wavelength. To achieve a balance between PPC and NPC under 406 nm or 520 nm light, a partially overlapping configuration was designed. For both EPSC and IPSC effects, In_2Se_3 plays a crucial role by facilitating photocarrier generation and by controlling interlayer charge separation and channel conductance through dipolar rearrangement. Furthermore, gate induced polarization reversal enables further electrical handle to control the optically induced PSC levels. The precise modulation of synaptic behaviours, achieved through both optical and hybrid optical-electrical inputs, underscores the device suitability for advanced neuromorphic vision systems. This was demonstrated by utilizing the bidirectional photoresponse for reconfigurable optical-write optical-erase logic platform and image recognition functionality, showcasing its versatility for next-generation neuromorphic hardware systems, on chip optical communication and optoelectronic applications at the nanoscale level.

Experimental section

Sample Preparation

In_2Se_3 (HQ Graphene) flakes were directly exfoliated onto a pre-patterned SiO_2 surface using the conventional scotch tape exfoliation method. The first few layers of In_2Se_3 were removed from the bulk crystal to eliminate surface oxide layers and minimize undesirable contamination. Few layers of $PdSe_2$ (HQ Graphene) were exfoliated onto a PDMS stamp, which was mounted on a glass slide. An optical microscope (Olympus BX53M) equipped with a digital camera (Olympus UC90) was employed to identify suitable flakes. Using a dry transfer technique, selected $PdSe_2$ flakes were precisely aligned and transferred onto the In_2Se_3 surface with the aid of an XYZ micro-manipulator stage attached to the optical microscope.

Device Fabrication

A standard electron beam lithography (EBL) technique was employed to define the metal contacts for the drain and source electrodes on the $PdSe_2$ layer using 950K-poly (methyl

View Article Online
DOI: 10.1039/D5MH02349A

methacrylate) (PMMA) resist. After the development of the resist the sample was placed under mild oxygen plasma (Diener PCCE) of 50 W for ~5 seconds to remove unwanted resist residuals. Subsequently, 5 nm Cr and 60 nm Au were deposited on the sample by electron beam evaporation (Evatec BAK 501A) to serve as electrodes followed by a lift-off process. The deposition rate was set to ~0.5 Å/s for Cr and to ~1 Å/s for Au at the base pressure of ~7 × 10^{-7} Torr.

Materials Characterization

Standard optical microscope (Olympus BX53M) was used to identify suitable flakes after exfoliation. Morphological study of the device was carried out by Bruker Dimension-Icon Atomic Force Microscopy (AFM) in tapping mode inside a N_2 filled glovebox (H_2O and O_2 content <1 ppm). PFM measurements were conducted under ambient conditions using an Asylum Research/Oxford Instruments MFP-3D Infinity AFM system equipped with a conductive Pt/Ir-coated cantilever (PPP-EFM-50, NANOSENSORS™). In_2Se_3 flakes were mechanically exfoliated onto a conductive substrate comprising 5 nm Cr/50 nm Au deposited on a p^{++} Si/SiO_2 wafer. The tip was operated in contact mode (resonance frequency ~290 kHz) to scan two square regions of different sizes. During scanning, bias voltage of +6V and -6V was applied to the tip while the conductive surface was grounded. VECTOR PFM mode was used to characterize the OOP ferroelectric domains with a drive amplitude of 3V and 1 Hz scan rate. Spectroscopic characterization of the 2D layers and their heterostructure was carried out using Raman spectrometer (WITec Alpha300R). The measurements were carried out in confocal mode using a 532 nm laser with 100× objective (NA = 0.9; $\Delta\lambda \approx 360$ nm, 1800 g mm^{-1} grating) lens. The excitation power was typically ~1 mW to avoid any heating and material degradation. SPCM measurements were carried out with same Raman spectrometer setup. The device was scanned with an excitation power of 0.3 mW with a 50× objective (NA = 0.45) lens. An optical chopper (Thorlabs, MC1F10HP) at a frequency of 1500 Hz and a lock in amplifier (Zurich Instruments, MFLI) were used to probe the photocurrent.

Optoelectronic characterization

Electrical and optoelectronic characterization of the fabricated devices were carried out in ambient conditions using a semiconductor parameter analyzer unit (Keysight B1500A) and a probe station (Semishare, SM-4) equipped with an optical microscope. The synaptic measurements were performed using a 4-channel fiber-coupled pulse laser source (model-MCLS1, Thorlabs) focused through a multimode fiber (400 μm core, NA=0.39, model: M74L, Thorlabs) and series of adjustable aspheric collimators (models: CFC2-A, CFC2-b and CFC2-C; Thorlabs). Different wavelengths (406 nm, 520 nm, 642 nm, 785 nm, 980 nm) of varying intensities ($P_{d,\ 406\ nm}$: 0.13 – 0.19 mW/mm^2, $P_{d,\ 520\ nm}$: 0.61 mW/mm^2, $P_{d,\ 642\ nm}$: 0.04 – 0.47 mW/mm^2, $P_{d,\ 785\ nm}$: 0.35 mW/mm^2, $P_{d,\ 980nm}$: 0.18 mW/mm^2) and pulse width input signals were used for synaptic measurements. The frequency of laser pulses was modulated with an externally feed-in square waveform generator (Keysight 336000A).

AUTHOR INFORMATION

Corresponding Author

View Article Online
DOI: 10.1039/D5MH02349A

Elad Koren – *Nanoscale Electronic Materials and Devices Laboratory, Faculty of Materials Science and Engineering, Technion - Israel Institute of Technology, Haifa 3200003, Israel.*
Email: eladk@technion.ac.il

Authors

Anurag Ghosh – *Nanoscale Electronic Materials and Devices Laboratory, Faculty of Materials Science and Engineering, Technion - Israel Institute of Technology, Haifa 3200003, Israel.*

Inbar Dahan – *Nanoscale Electronic Materials and Devices Laboratory, Faculty of Materials Science and Engineering, Technion - Israel Institute of Technology, Haifa 3200003, Israel.*

Bisweswar Santra – *Nanoscale Electronic Materials and Devices Laboratory, Faculty of Materials Science and Engineering, Technion - Israel Institute of Technology, Haifa 3200003, Israel.*

Gautham Vijayan – *Nanoscale Electronic Materials and Devices Laboratory, Faculty of Materials Science and Engineering, Technion - Israel Institute of Technology, Haifa 3200003, Israel.*

Michael Uzhansky – *Nanoscale Electronic Materials and Devices Laboratory, Faculty of Materials Science and Engineering, Technion - Israel Institute of Technology, Haifa 3200003, Israel.*

ACKNOWLEDGMENTS

E.K. gratefully acknowledges the Israel Department of Energy, the Ministry of Innovation, Science & Technology and the "Ray and Miriam Klein" research foundation for financial support.

References

1. Migliato Marega, G. *et al.* Logic-in-memory based on an atomically thin semiconductor. *Nature* **587**, 72–77 (2020).
2. Mukherjee, S., Dutta, D., Ghosh, A. & Koren, E. Graphene-In2Se3 van der Waals Heterojunction Neuristor for Optical In-Memory Bimodal Operation. *ACS Nano* **17**, 22287–22298 (2023).
3. Zhang, T. *et al.* A Reconfigurable All-Optical-Controlled Synaptic Device for Neuromorphic Computing Applications. *ACS Nano* **18**, 16236–16247 (2024).
4. Hadke, S., Kang, M.-A., Sangwan, V. K. & Hersam, M. C. Two-Dimensional Materials for Brain-Inspired Computing Hardware. *Chem. Rev.* https://doi.org/10.1021/acs.chemrev.4c00631 (2025) doi:10.1021/acs.chemrev.4c00631.
5. Wang, C.-Y. *et al.* Gate-tunable van der Waals heterostructure for reconfigurable neural network vision sensor. *Science Advances* **6**, eaba6173.
6. Zhou, F. *et al.* Optoelectronic resistive random access memory for neuromorphic vision sensors. *Nature Nanotechnology* **14**, 776–782 (2019).
7. Hou, Y.-X. *et al.* Large-Scale and Flexible Optical Synapses for Neuromorphic Computing and Integrated Visible Information Sensing Memory Processing. *ACS Nano* **15**, 1497–1508 (2021).
8. Li, H. *et al.* Fully photon modulated heterostructure for neuromorphic computing. *Nano Energy* **65**, 104000 (2019).
9. Zeng, J. *et al.* Multisensory Ferroelectric Semiconductor Synapse for Neuromorphic Computing. *Advanced Functional Materials* **34**, 2313010 (2024).
10. Du, J. *et al.* A robust neuromorphic vision sensor with optical control of ferroelectric switching. *Nano Energy* **89**, 106439 (2021).
11. Feng, P. *et al.* Self-Powered Optoelectronic Synaptic Devices Based on In2Se3/MoS2 Ferroelectric Heterojunction with Boosted Performance. *Advanced Materials Technologies* **9**, 2301355 (2024).
12. Li, X. *et al.* Multi-Functional Platform for In-Memory Computing And Sensing Based on 2D Ferroelectric Semiconductor α-In2Se3. *Advanced Functional Materials* **34**, 2306486 (2024).

View Article Online
DOI: 10.1039/D5MH02349A

13. Hu, L. *et al.* Emerging Optoelectronic Devices for Brain-Inspired Computing. *Advanced Electronic Materials* **n/a**, 2400482 (2024).

14. Sun, J. *et al.* Optoelectronic Synapse Based on IGZO-Alkylated Graphene Oxide Hybrid Structure. *Advanced Functional Materials* **28**, 1804397 (2018).

15. Chen, Y. *et al.* Bidirectional Synaptic Phototransistor Based on Two-Dimensional Ferroelectric Semiconductor for Mixed Color Pattern Recognition. *ACS Nano* **17**, 12499–12509 (2023).

16. Wang, Y. *et al.* Negative Photoconductance in van der Waals Heterostructure-Based Floating Gate Phototransistor. *ACS Nano* **12**, 9513–9520 (2018).

17. Seo, S. *et al.* Artificial optic-neural synapse for colored and color-mixed pattern recognition. *Nature Communications* **9**, 5106 (2018).

18. Yang, R. *et al.* All-Optically Controlled Artificial Synapse Based on Full Oxides for Low-Power Visible Neural Network Computing. *Advanced Functional Materials* **34**, 2312444 (2024).

19. Zhu, X. & Lu, W. D. Optogenetics-Inspired Tunable Synaptic Functions in Memristors. *ACS Nano* **12**, 1242–1249 (2018).

20. Yang, C. M. *et al.* Bidirectional All-Optical Synapses Based on a 2D Bi2O2Se/Graphene Hybrid Structure for Multifunctional Optoelectronics. *Adv. Funct. Mater.* **30**, 2001598 (2020).

21. Wang, L. *et al.* Negative Photoconductivity Transistors for Visuomorphic Computing. *Advanced Materials* **36**, 2403538 (2024).

22. Ge, S. *et al.* Bidirectional Photoresponse in Perovskite-ZnO Heterostructure for Fully Optical-Controlled Artificial Synapse. *Advanced Optical Materials* **10**, 2200409 (2022).

23. Li, X. *et al.* Light-Induced Conductance Potentiation and Depression in an All-Optically Controlled Memristor. *ACS Appl. Mater. Interfaces* **16**, 27866–27874 (2024).

24. Zhou, F., Chen, J., Tao, X., Wang, X. & Chai, Y. 2D Materials Based Optoelectronic Memory: Convergence of Electronic Memory and Optical Sensor. *Research* **2019**, 2019/9490413 (2019).

25. Chen, H. *et al.* Logic gates based on neuristors made from two-dimensional materials. *Nature Electronics* **4**, 399–404 (2021).

View Article Online
DOI: 10.1039/D5MH02349A

26. Ahmed, T. *et al.* Fully Light-Controlled Memory and Neuromorphic Computation in Layered Black Phosphorus. *Adv. Mater.* **33**, 2004207 (2021).
27. Jiang, J. *et al.* Wavelength-Controlled Photoconductance Polarity Switching via Harnessing Defects in Doped PdSe2 for Artificial Synaptic Features. *Small* **20**, 2306068 (2024).
28. Lian, Y. *et al.* Tunable Bi-directional Photoresponse in Hybrid PtSe2− Thin Films Based on Precisely Controllable Selenization Engineering. *Advanced Functional Materials* **32**, 2205709 (2022).
29. Katznelson, S. *et al.* Bright excitonic multiplexing mediated by dark exciton transition in two-dimensional TMDCs at room temperature. *Mater. Horiz.* **9**, 1089–1098 (2022).
30. Liang, Q., Chen, Z., Zhang, Q. & Wee, A. T. S. Pentagonal 2D Transition Metal Dichalcogenides: PdSe2 and Beyond. *Advanced Functional Materials* **32**, 2203555 (2022).
31. Liang, Q. *et al.* High-Performance, Room Temperature, Ultra-Broadband Photodetectors Based on Air-Stable PdSe2. *Advanced Materials* **31**, 1807609 (2019).
32. Xia, Y. *et al.* 2D Reconfigurable Memory Device Enabled by Defect Engineering for Multifunctional Neuromorphic Computing. *Advanced Materials* **36**, 2403785 (2024).
33. Gao, J. *et al.* Multifunctional MoTe2 Fe-FET Enabled by Ferroelectric Polarization-Assisted Charge Trapping. *Advanced Functional Materials* **32**, 2110415 (2022).
34. Pervez, M. H. *et al.* Recent Developments on Novel 2D Materials for Emerging Neuromorphic Computing Devices. *Small Structures* **6**, 2400386 (2025).
35. Joo, Y., Hwang, E., Hong, H., Cho, S. & Yang, H. Memory and Synaptic Devices Based on Emerging 2D Ferroelectricity. *Advanced Electronic Materials* **9**, 2300211 (2023).
36. Liu, K. *et al.* An optoelectronic synapse based on α-In2Se3 with controllable temporal dynamics for multimode and multiscale reservoir computing. *Nat Electron* **5**, 761–773 (2022).
37. Wang, L. *et al.* Exploring Ferroelectric Switching in α-In2Se3 for Neuromorphic Computing. *Advanced Functional Materials* **30**, 2004609 (2020).

View Article Online
DOI: 10.1039/D5MH02349A

38. Gao, J. *et al.* Intrinsic polarization coupling in 2D α-In2Se3 toward artificial synapse with multimode operations. *SmartMat* **2**, 88–98 (2021).

39. Dutta, D., Mukherjee, S., Uzhansky, M. & Koren, E. Cross-field optoelectronic modulation via inter-coupled ferroelectricity in 2D In2Se3. *npj 2D Mater Appl* **5**, 81 (2021).

40. Zhou, Y. *et al.* Out-of-Plane Piezoelectricity and Ferroelectricity in Layered α-In $_2$ Se $_3$ Nanoflakes. *Nano Lett.* **17**, 5508–5513 (2017).

41. Mukherjee, S., Dutta, D., Uzhansky, M. & Koren, E. Monolithic In2Se3–In2O3 heterojunction for multibit non-volatile memory and logic operations using optoelectronic inputs. *npj 2D Materials and Applications* **6**, 37 (2022).

42. Mukherjee, S. *et al.* Scalable Integration of Coplanar Heterojunction Monolithic Devices on Two-Dimensional In2Se3. *ACS Nano* **14**, 17543–17553 (2020).

43. Mukherjee, S. & Koren, E. Indium Selenide (In2Se3) – An Emerging Van-der-Waals Material for Photodetection and Non-Volatile Memory Applications. *Israel Journal of Chemistry* **62**, e202100112 (2022).

44. Li, M. *et al.* Defect Engineering in Ambipolar Layered Materials for Mode-Regulable Nociceptor. *Advanced Functional Materials* **31**, 2007587 (2021).

45. Dutta, D. *et al.* Edge-Based Two-Dimensional α-In2Se3–MoS2 Ferroelectric Field Effect Device. *ACS Appl. Mater. Interfaces* **15**, 18505–18515 (2023).

46. Uzhansky, M., Mukherjee, S., Vijayan, G. & Koren, E. Non-Volatile Reconfigurable p–n Junction Utilizing In-Plane Ferroelectricity in 2D WSe2/α-In2Se3 Asymmetric Heterostructures. *Advanced Functional Materials* **34**, 2306682 (2024).

47. Uzhansky, M., Rakshit, A., Kalcheim, Y. & Koren, E. Coupled pyroelectric-photovoltaic effect in 2D ferroelectric α-In2Se3. *npj 2D Materials and Applications* **9**, 6 (2025).

48. Guo, F. *et al.* Achieving reinforcement learning in a three-active-terminal neuromorphic device based on a 2D vdW ferroelectric material. *Mater. Horiz.* **10**, 3719–3728 (2023).

View Article Online
DOI: 10.1039/D5MH02349A

49. Wan, S. *et al.* Room-temperature ferroelectricity and a switchable diode effect in two-dimensional α-In2Se3 thin layers. *Nanoscale* **10**, 14885–14892 (2018).

50. Zhou, Y. *et al.* Out-of-Plane Piezoelectricity and Ferroelectricity in Layered α-In2Se3 Nanoflakes. *Nano Lett.* **17**, 5508–5513 (2017).

51. Zheng, C. *et al.* Room temperature in-plane ferroelectricity in van der Waals In_2Se_3. *Science Advances* **4**, eaar7720 (2018).

52. Xue, F. *et al.* Room-Temperature Ferroelectricity in Hexagonally Layered α-In2Se3 Nanoflakes down to the Monolayer Limit. *Advanced Functional Materials* **28**, 1803738 (2018).

53. Io, W. F. *et al.* Temperature- and thickness-dependence of robust out-of-plane ferroelectricity in CVD grown ultrathin van der Waals α-In2Se3 layers. *Nano Research* **13**, 1897–1902 (2020).

54. Hoffman, A. N. *et al.* Exploring the air stability of PdSe2 via electrical transport measurements and defect calculations. *npj 2D Materials and Applications* **3**, 50 (2019).

55. Grillo, A. *et al.* Coexistence of Negative and Positive Photoconductivity in Few-Layer PtSe2 Field-Effect Transistors. *Advanced Functional Materials* **31**, 2105722 (2021).

56. Han, S. S. *et al.* Wafer-Scale Anion Exchange Conversion of Nonlayered PtS Films to van der Waals Two-Dimensional PtTe2 Layers with Negative Photoresponsiveness. *Chem. Mater.* **34**, 6996–7005 (2022).

57. Han, S. S. *et al.* Wafer-scale flexible 2D PtSe2 layers with bi-directional wavelength tunability for fully optical synaptic operations. *Nano Energy* **139**, 110943 (2025).

58. Poh, S. M. *et al.* Molecular-Beam Epitaxy of Two-Dimensional In2Se3 and Its Giant Electroresistance Switching in Ferroresistive Memory Junction. *Nano Lett.* **18**, 6340–6346 (2018).

59. Mu, Y. *et al.* Homo-type α-In2Se3/PdSe2 Ferroelectric van der Waals Heterojunction Photodetectors with High-performance and Broadband. *Advanced Functional Materials* **34**, 2315543 (2024).

View Article Online
DOI: 10.1039/D5MH02349A

60. Kim, H. & Choi, H. J. Quasiparticle band structures of bulk and few-layer \mathrmPdSe_2 from first-principles GW calculations. *Phys. Rev. B* **103**, 165419 (2021).

61. Zidan, M. A., Strachan, J. P. & Lu, W. D. The future of electronics based on memristive systems. *Nature Electronics* **1**, 22–29 (2018).

62. Ryu, J. J. *et al.* Highly Linear and Symmetric Weight Modification in HfO2-Based Memristive Devices for High-Precision Weight Entries. *Advanced Electronic Materials* **6**, 2000434 (2020).